

Carbon-phosphorus-nitrogen materials as highly thermally stable catalyst supports for CO₂ hydrogenation to methanol

*Adi Azoulay^a, Alberto Garcia Baldovi^b, Josep Albero^b, Noa Azaria^c, Jonathan Tzadikov^a, Ayelet Tashakory^a, Neeta Karjule^a, Shmuel Hayun^c, Hermenegildo García^b, and Menny Shalom^{*a}*

^aDepartment of Chemistry and Ilse Katz Institute for Nanoscale Science and Technology, Ben-Gurion University of the Negev, Beer-Sheva 8410501, Israel.

^bInstituto Universitario Mixto de Tecnología Química (UPV-CSIC), Universitat Politècnica de València, Avda. de los Narajos s/n, 46022, Valencia, Spain.

^cDepartment of Materials Engineering, Ben-Gurion University of the Negev, Beer-Sheva, Israel.

Keywords: Supramolecular assembly, metal-free material design, Cu-Fe catalyst, thermally stable catalyst support, CO₂ hydrogenation to methanol, heterogenous catalysis

ABSTRACT: The direct conversion of CO₂ into methanol through hydrogenation reactions by heterogeneous catalysts is considered a promising green approach for fuel production. The

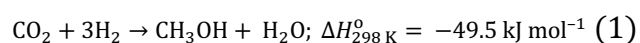
most researched catalyst for methanol formation is Cu, usually in combination with other metals, dispersed on different substrates. However, several challenges, such as the low stability, activity, and selectivity of the catalyst hinder further progress. Here we present catalysts consisting of Cu and Fe nanoparticles deposited on lightweight carbon-phosphorous-nitrogen (CPN) materials as the support for CO₂ hydrogenation to methanol. Detailed analysis reveals a correlation between the elemental composition of the CPN supports and their CO₂ adsorption capability, which benefits CO₂ conversion to methanol. The unique elemental composition ensures uniform dispersion of both Cu and Fe nanoparticles on CPN and prevents the oxidation of the Cu active sites during the reaction. The best performing of the catalysts exhibits a remarkable methanol production yield of 9.82 mol kg_{cat}⁻¹ h⁻¹ at 250 °C under 20 bars, with good methanol selectivity, negligible CO formation, and good stability for 12 h under harsh conditions.

Introduction

The development of sustainable and renewable carbon-neutral fuels and chemicals has been proposed as an appealing approach to mitigate CO₂ emissions.¹ The direct conversion of CO₂ into liquid fuels, such as methanol, through hydrogenation reactions using H₂ has attracted massive attention. Several pilot plants based on this approach have already been installed, with production capacities as high as 45,000 t/year.^{2,3}

Methanol is among the top ten commodity chemicals (30 × 10⁶ Mt/year)⁴, and it is typically produced in the industry at high temperatures (200–300 °C) and pressures (5–10 MPa) to

achieve cost-effective conversion rates. Catalytic CO₂ hydrogenation (Equation 1) is considered impractical for industrial use, owing to the poor activity of the relevant catalysts. Moreover, competitive reactions occur in parallel at low temperatures and high pressures, particularly CO formation through the reverse water–gas shift reaction.^{5–8} Therefore, highly efficient and robust catalysts are needed to increase the reaction rate and selectivity.



The most widely used catalyst for methanol synthesis via CO₂ hydrogenation has been Cu/ZnO/Al₂O₃^{9,10}, although a large variety of Cu-based catalysts supported on different metal oxides (e.g., Cu/ZnO/ZrO, Cu/CeO₂/TiO, and Pd-Cu/SiO₂), graphene-based materials, and MOFs have been investigated.^{11–13} Nevertheless, the catalytic performance of these Cu-based catalysts is still unsatisfactory because of the simultaneous formation of water (Eq. 1) as by-product promoting sintering and oxidation of the Cu active sites during the reaction, which leads to catalyst deactivation.^{14,15} Besides, high Cu loadings also promote sintering, which limits the Cu content on the support.¹⁶ Finally, CO is typically produced as a consequence of the reverse water–gas shift reaction occurring in parallel to the hydrogenation of CO₂ to methanol at low temperatures.¹⁷ For these reasons, the design of new catalysts exhibiting high activity, selectivity, water tolerance, and stability is essential for the industrial development of CO₂ hydrogenation to methanol.¹⁸ Over the last few years, metal-free materials have received considerable attention as catalyst supports owing to their favorable properties, such as high specific surface area, high mechanical strength, and strong metal–support interaction, which promote better metal dispersion and improve stability.^{12,19–21} We recently reported the

preparation of phosphorous-nitrogen-carbon materials with controllable elemental composition and structural, electronic, and thermal stability.²² These materials exhibit remarkable stability up to 970 °C in air and may be suitable for use as sustainable lightweight supports for metal-based catalysts.

The present study shows that Cu and Fe nanoparticles deposited on lightweight carbon-phosphorous-nitrogen materials exhibit excellent activity as catalysts for CO₂ hydrogenation to methanol, along with good stability. Our results show a high methanol production rate of 1.53 mol of MeOH kg_{cat}⁻¹ h⁻¹ at 250 °C and under 20 bar, with notable stability of the catalyst and minor decay in the yield over the time. HRTEM analysis before and after the reaction revealed minor changes in the Cu and Fe nanoparticle morphology and oxidation state. This improved stability, which we attribute to a strong metal–support interaction, makes this catalyst support suitable to stand harsh conditions of the CO₂ hydrogenation to methanol.

Materials and methods

Materials. Melamine (99%, Alfa Aesar), Orthophosphoric acid (H₃PO₄ 85 wt%, Bio-Lab Chemicals), 2-propanol (LOBA Chemie), nitric acid (HNO₃ 67–69 wt%, trace metal grade, Fisher Chemical), copper(II) nitrate trihydrate (purum p.a., 98.0–103%, Sigma–Aldrich), Iron(III) nitrate nonahydrate (99+%, Acros Organics), and acetone (Bio-Lab AR grade) were used without further purification. Deionized water was purified using a Millipore Direct-Q3 water purification system (18.2 MΩ cm resistivity) and was used as a solvent in all experiments.

Synthetic procedures of carbon-phosphorus-nitrogen composites. First, MPA_x crystalline precursors were prepared by dissolving 2 g of melamine in 150 mL of DI water, followed by the addition of certain amounts of phosphoric acid (85 wt% in H_2O) to obtain molar ratios of 1:2, 1:1, and 2:1 (melamine: H_3PO_4). The reaction mixtures were then placed on a pre-heated heating plate (85 °C) and mixed thoroughly. After 1 h reaction time, each mixture was naturally cooled down to room temperature for another 1 h, and filtered to extract the corresponding MPA_x supramolecular precursor. All MPA_x precursors were washed three times with water and then acetone.

The MPA_x precursors were transferred to lidded ceramic crucibles and calcined under N_2 atmosphere in a muffled furnace. The calcination process started by heating the precursors to 90 °C for 1 h to remove impurities. The temperature was then gradually increased to 800 °C at a constant heating ramp of 3 °C min^{-1} . Lastly, the precursors were kept at this temperature for 4h to complete the condensation procedure.

Cu and Fe deposition on CPN_1 . CuFe/CPN_1 catalyst was synthesized by dispersing 100 mg of CPN_1 in 20 mL MilliQ water using a tip sonicator (400W) for 0.5 h. An aqueous solution of copper(II) nitrate trihydrate was prepared by dissolving 7.5 wt% Cu in MilliQ water. The obtained solution was then added dropwise to the CPN_1 dispersion and kept under continuous stirring overnight at 60 °C to ensure water evaporation. After drying the resulted Cu(II)-CPN_1 at 100 °C for 3 h, it was thermally reduced to $\text{Cu}^0\text{-CPN}_1$ under $\text{H}_2:\text{N}_2$ (5:95, v/v) environment at 350 °C for 3 h (heating ramp of 10 °C min^{-1}). The reduced Cu/CPN_1 was impregnated with Fe(III) by using iron (III) nitrate nonahydrate aqueous solution containing 5 wt% of Fe in the

same manner. CuFe/CPN₁ was then washed with water and acetone to eliminate metallic salts residues.

Characterizations. XRD experiments were performed using a PANalytical's Empyrean diffractometer equipped with a position-sensitive detector X'Celerator. FTIR measurements were carried out on a Thermo Scientific Nicolet iS5 FTIR spectrometer equipped with a Si ATR. Nitrogen adsorption–desorption isotherm measurements were conducted at –196 °C using an ASAP 2020 (Micrometrics, Norcross, GA) instrument. The surface areas were measured by the Brunauer–Emmett–Teller (BET) method. Ten-point adsorption isotherms of nitrogen were collected in the P/P_0 relative pressure range (P_0 = saturation pressure) of 0.05–0.30; pore diameter and volume were calculated using the Barrett-Joyner-Halenda (BJH) method. Prior to analysis, each sample was degassed under vacuum at 150 °C for 8 h. CO₂ full isotherm measurements were obtained using the same instrument at 25 °C. The CO₂ adsorption–desorption data were collected in the range of 0–800 mmHg (absolute pressure). Prior to analysis, each sample was degassed under vacuum at 150 °C for 8 h.

SEM images of MPA_x supramolecular assemblies and CPN_x materials after calcination were captured using a FEI Verios 460L high-resolution SEM equipped with a FEG 2S source and operated at 3.0 kV for imaging. All SEM samples were sputtered with gold (Au) before analysis. A JEOL JEM-2100F analytical TEM operated at 200 kV was used for HRTEM imaging, Scanning TEM (STEM) and EDS analysis. STEM was performed using a GATAN 806 HAADF (high-angle annular dark-field) STEM detector. EDS was performed using a JED-2300T energy

dispersive X-ray spectrometer. The probe size during the analysis was set to 1 nm. The software JEOL Analytical Station (v. 3.8.0.21) was used to analyze the EDS data.

XPS was performed with a Thermo Fisher Scientific ESCALAB 250 using monochromated K α X-rays (1486.6 eV). The data was collected with a scanning time of ca. 7 min over a 2θ range of 5° to 60° using Cu K α radiation ($\lambda = 1.54178 \text{ \AA}$, 40 kV, 30 mA). Elemental analysis data for carbon, nitrogen, and hydrogen (CNH) was collected using a Thermo Scientific Flash Smart elemental analyzer OEA 2000. Samples for inductively-coupled plasma optical emission spectrometry (ICP OES) were prepared by dissolution in concentrated nitric acid in a PTFE-lined autoclave for 8 h at 180 °C and were then analyzed using a Spectro ARCOS ICP-OES, FHX22 multi-view plasma instrument (radial configuration). All MAS NMR experiments were carried out on a Bruker Avance III 500 MHz narrow-bore spectrometer, using a 4 mm double-resonance MAS probe at a spinning rate of 8 KHz. ^{13}C CP MAS experiments were carried out using a 2.5 μs ^1H 90° pulse, a 2 ms mixing time, and a 3 s recycle delay between acquisitions. ^{31}P CP MAS experiments were carried out using a 2.5 μs ^1H 90° pulse, 3 ms mixing time and a 5 s recycle delay between acquisitions. ^{31}P direct excitation experiments were carried out with use of a 3.860 μs 90° pulse and a recycle delay of 15 s.

CO $_2$ hydrogenation to methanol set-up: CO $_2$ hydrogenation experiments were carried out in a pressurized stainless steel fixed bed reactor under continuous gas flow of a diluted CO $_2$:H $_2$ mixture (3:1, v:v). The evolved gases were analyzed using a gas chromatography-mass spectrophotometer from Agilent (QP 6890 N) containing an HP5 column and EM detector

(from 5 to 700 uam), and the products were quantified by gas chromatography using a Varian 3900 with FID detector and HP5 column, TRB-5, 30 m length and 0.25×0.25.

Results and Discussion

Characterization of melamine-phosphoric acid supramolecular precursors. MPA_x precursors (M stands for melamine, PA for phosphoric acid, and $x = 2, 1, \text{ or } 0.5$ represents the molar ratio between melamine and phosphoric acid) were prepared by mixing melamine and phosphoric acid monomers in an aqueous solution for 1 h at 85 °C, then cooling the mixture to room temperature for another 1 h to complete the crystallization process. After filtration, the MPA_x crystals were washed several times with water and acetone to remove unreacted residues. The altered molar ratio of the starting monomers strongly affects the composition of the MPA_x precursors and their crystal structure, which leads to significant changes in their X-ray diffraction (XRD) spectra (Figure 1a).²² Fourier transform infrared (FTIR) measurements of the MPA_x precursors reveal the establishment of a hydrogen-bonded supramolecular framework (Figure 1b), as evidenced by the disappearance of the two sharp peaks at 3420, and 3470 cm^{-1} corresponding to the free amine groups in melamine.

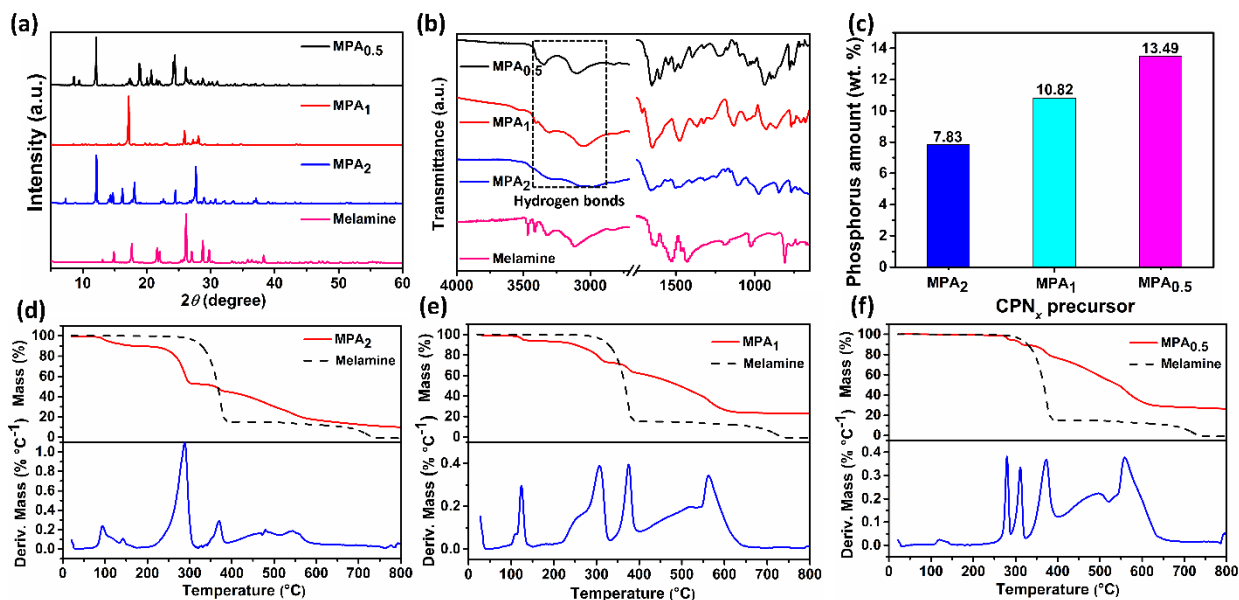
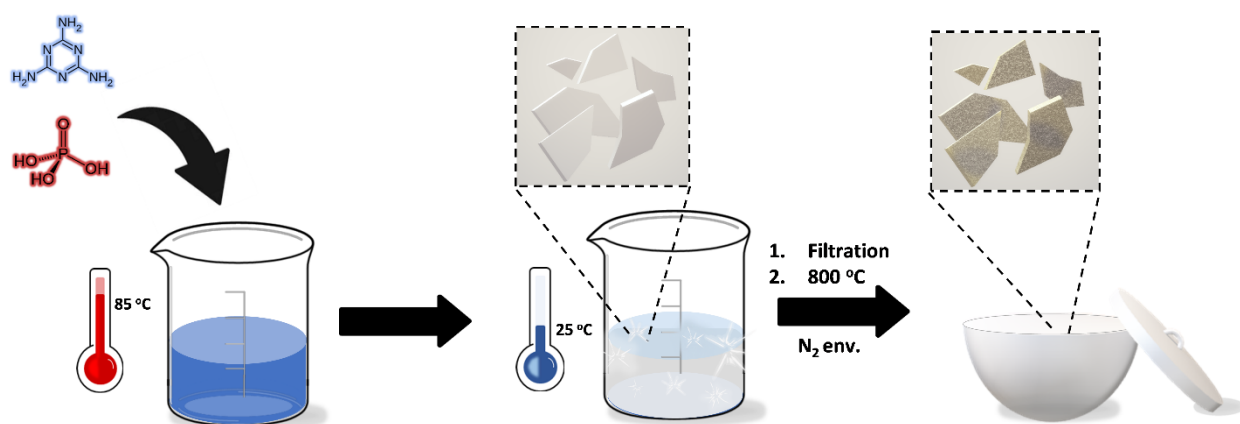


Figure 1. (a) XRD patterns and (b) FTIR spectra of MPA_x precursors and melamine. (c) Phosphorous concentrations (wt%) in MPA_x, provided by ICP-OES and their (d–f) TGA profiles under a N₂ environment.

Inductively-coupled plasma optical emission spectroscopy (ICP-OES) and elemental analysis (EA) measurements of the MPA_x supramolecular precursors show that the elemental composition in the final crystal is controlled by the starting M:PA molar ratio (Figure 1c and Table S1). Indeed, a more elevated phosphorus content and lower carbon and nitrogen concentrations were obtained in the MPA_x precursor, prepared with a lower M:PA molar ratio. The thermogravimetric analysis (TGA) curve of MPA₂ implies that when melamine is in excess, its self-condensation is favored at the expense of condensation with phosphoric acid, resulting in a significant mass loss at 290 °C (Figure 1d).²³ Meanwhile, the TGA profiles of both MPA₁ and MPA_{0.5} show their superior thermal stability during calcination and higher mass

yields of 23 and 26%, respectively. This lesser mass loss is probably due to an increased number of interactions between melamine and phosphoric acid, which disfavors melamine sublimation (Figure 1e, 1f).

Scanning electron microscopy (SEM) images of the MPA_x supramolecular precursors reveal smooth and ordered structures, where the initial M:PA molar ratio determines the shape of each precursor crystal (Figure 2a–c).



Scheme 1. Preparation of MPA_1 supramolecular aggregate, followed by calcination at 800 °C to form CPN_1 .

Characterization of Carbon-phosphorus-nitrogen materials. Carbon-phosphorus-nitrogen (CPN_x , where x is the initial M:PA molar ratio) materials were prepared by thermal treatment of MPA_x precursors at 800 °C for 4 h under a nitrogen environment to ensure full condensation and the formation of thermally stable P–N bonds within the structure (the complete synthetic procedure is illustrated in scheme 1). The well-defined size and shape of the precursor enable the transfer of their macrostructures to the final CPN_x materials, as shown in the SEM images (Figure 2d–f). This observation agrees with previous reports, which demonstrate the merit of

using supramolecular crystalline materials as precursors to control the structure of the final materials.^{22,24,25} The XRD patterns of the CPN_x display signals corresponding to an amorphous structure, with a single broad diffraction peak located at 23.1° (Figure S1a). FTIR spectra confirmed the formation of a polyphosphazene network: the C–O–P stretching vibration is visible at 750 cm⁻¹, and the stretching modes of phosphate groups, $\nu(\text{P–O–P})$ ²⁶ and $\nu(\text{P=O})$,²⁷ and heptazine units, $\nu(\text{C–N/C–N=C})$ ²⁸ can be seen at 915, 1222, and 2162 cm⁻¹, respectively (Figure S1b).

The elemental composition of the CPN_x materials is directly related to the distribution of P, N, and C in the precursors; nevertheless, their P content values are close to each other (Figure S1c and Table S2). The CPN_x materials mainly contain phosphorus and nitrogen elements after calcination at 800 °C. In contrast, the carbon content is low, owing to the formation of a thermodynamically favorable P–N network during the calcination process. X-ray photoelectron spectroscopy (XPS) P 2p spectra of CPN_x (Figure S2a) show two signals centered at 133.8–134.4 and 136.0–136.8 eV, the former corresponding to –N=P and –P–N species and the latter to oxidized phosphorus (PO_x).²⁹ The N 1s spectrum of CPN₁ reveals four peaks, at 397.5, 398.7, 399.7, and 401.0 eV, related to –N=P and –P–N species, pyridinic nitrogen group (C–N=C), neutral nitrogen (–NH–) and positively charged nitrogen (–NH⁺–), respectively (Figure S2b).^{30–32} These peaks indicating the formation of a polyphosphazene scaffold are observed in all CPN_x materials. C1s core-level spectra on the surface of CPN_x exhibit four peaks at 284.8, 286.4–286.6, 288.2–288.5, and 290.0–290.4 eV, assigned to sp² C–C, C–O, C=N–C, and O=C–O, respectively (Figure S2c).²² O1s spectra confirm the presence of all the oxide species

mentioned above, along with the addition of components attributed to the naturally adsorbed water molecules on the materials' surface (Figure S2d).³³

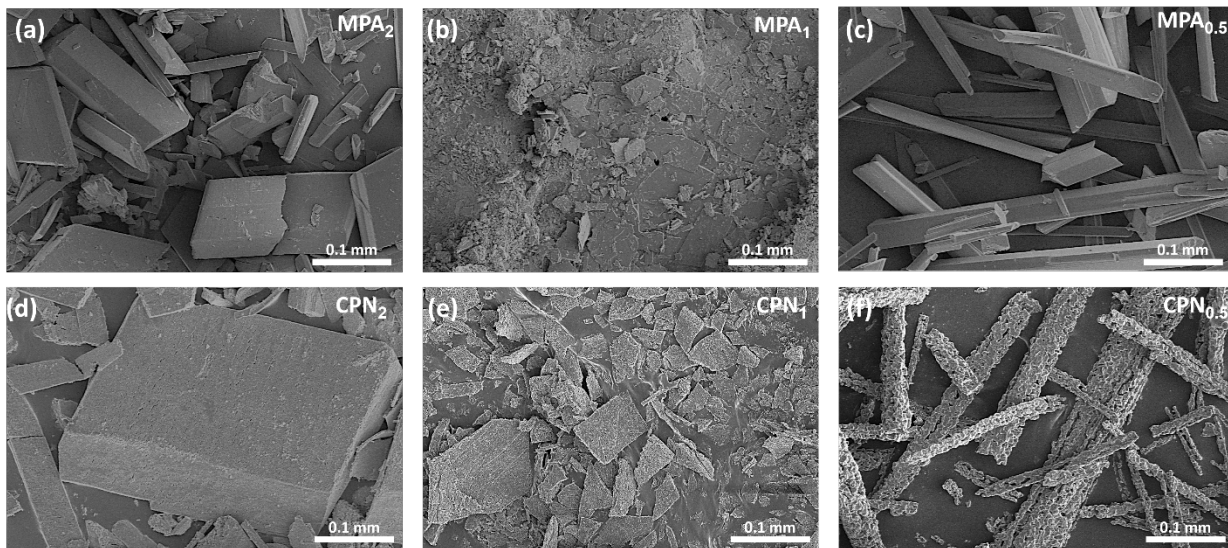


Figure 2. SEM images of (a–c) MPA_x crystalline precursors and (d–f) their corresponding products after calcination at 800 °C.

Adsorption properties. CO_2 full isotherms and N_2 sorption measurements of the CPNs show that they are made of mesoporous structures with considerable CO_2 capture capacity (Figure S3). CPN_2 shows the highest CO_2 uptake, 0.16 mmol g^{-1} , whereas CPN_1 and $\text{CPN}_{0.5}$ have slightly lower CO_2 capacities: 0.14 and 0.13 mmol g^{-1} , respectively. These values are similar to that reported for bulk polymerized ionic liquids (ca. 0.13 mmol g^{-1}), which are functional materials commonly used for CO_2 capture and separation.³⁴ In contrast with their CO_2 affinity, the CPN_x materials exhibit low specific surface areas as determined from N_2 sorption measurements (6.84 ± 0.06 , 5.64 ± 0.20 , and $3.77 \pm 0.08 \text{ m}^2 \text{ g}^{-1}$ for CPN_2 , CPN_1 , and $\text{CPN}_{0.5}$, respectively), suggesting that their elemental composition and/or the presence of ultramicropores are the main factors

behind their CO₂ adsorption capability (Table S3). The enhanced CO₂ uptake in CPN₂ could be related to its higher carbon content, which increases the surface polarity of the carbon-phosphorous-nitrogen-based material and thereby amplifies the uptake of CO₂.³⁵ Furthermore, CPN₂ displays a smaller BJH (Barrett-Joyner-Halenda) adsorption average pore width than CPN₁ and CPN_{0.5}, contributing to its superior CO₂ capture capacity.³⁶ Considering the low surface area of the CPNs, which reduces the adsorption uptake per contact area, these values of CO₂ adsorption are remarkably high.

Thermal stability of carbon-phosphorus-nitrogen. TGA studies of the CPN_x materials in air demonstrate their high thermal stability, a consequence of the large number of PN bonds within their structure (Figure S4). Although CPN₂ shows the highest CO₂ capacity, it presents the lowest oxidation resistance, with a 10% increase in material mass at 250 °C, which is likely due to the oxidation of surface carbon species. CPN₁ and CPN_{0.5} undergo a mass increase of 2 and 6% at the same temperature, respectively. These results highlight the good oxidation resistance of CPN₁ compared to the other CPNs, positioning it as the most suitable substrate for high-temperature catalysis, where self-oxidation plays a prominent role in catalyst deactivation.

Additional structural and morphological properties of CPN₁. We conducted ³¹P and ¹³C solid-state magic-angle spinning (MAS) nuclear magnetic resonance (NMR) experiments to elucidate the reaction pathway and analyze the CPN₁ material calcined at 800 °C (Figure S5 and Figure S6). To help with the former, we synthesized three intermediates at different calcination temperatures; 350, 450, and 550 °C. The ³¹P NMR spectrum of the MPA₁

supramolecular precursor shows three peaks from -1 to 4 ppm. According to the modeling we applied in our previous work, these peaks probably correspond to a phosphoric acid molecule attached to a deprotonated melamine unit.²² The CPN₁ 350 °C ³¹P NMR signals are shifted to more negative values, from -20 to -30 ppm, revealing the formation of P–N bonds during the calcination procedure.³⁷ After thermal treatment at higher temperatures (450 and 550 °C), a unique broad signal was recorded, at a negative shift, indicating the amorphous nature of the sample, which probably consists of a mixture of different PN_xO_{4-x} species. The ³¹P NMR spectrum of CPN₁ calcined at 800 °C shows three sharp peaks centered around 0 , 10 , and 23 ppm. These characteristic peaks are attributed to orthophosphate, pyrophosphate, and polyphosphate functional groups, respectively, and further corroborate the condensation of phosphoric acid and melamine molecules within the MPA₁ precursor into a fully polymerized structure.³⁸ The ¹³C solid-state NMR spectrum of MPA₁ and those of the CPN₁ intermediates display two main signal groups around 158 and 164 ppm, corresponding to triazine carbon (C–N₃) and carbon attached to amine groups (C–NH_x), respectively. In congruence with the ICP results, no signal was detected in the ¹³C NMR spectrum of CPN₁ 800 °C, owing to the negligible carbon content of the sample.

High-resolution transmission electron microscope (HRTEM) images of CPN₁ indicate the formation of an amorphous structure (Figure 3a). High-angle annular dark-field (HAADF-STEM) reveals that the material consists of macroporous structures of different sizes throughout the sample, which agrees with the CO₂ adsorption isotherms (Figure 3b). Figure

3c–f also support the formation of a carbon-nitrogen-phosphorous scaffold, each element being homogeneously distributed throughout the sample.

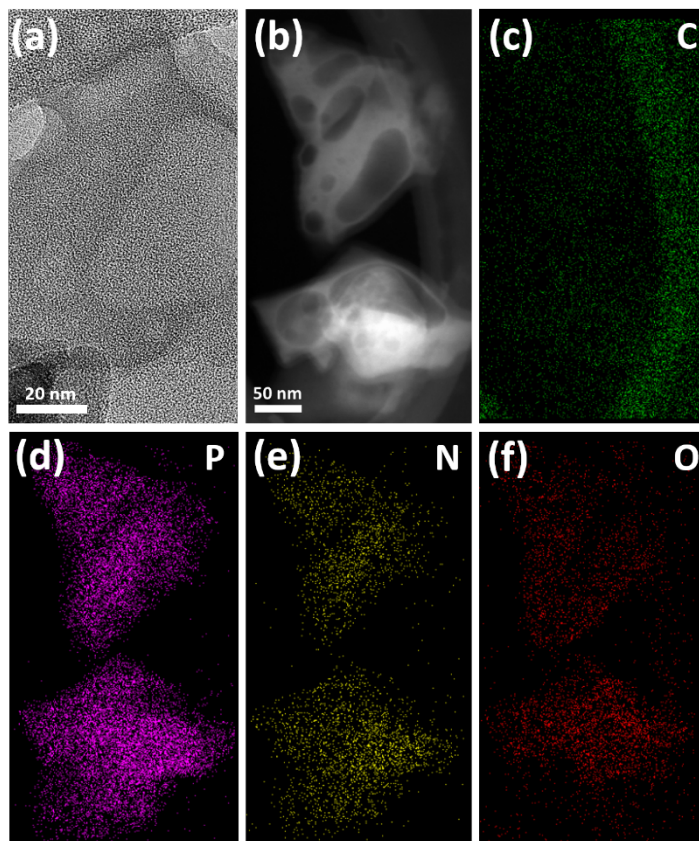


Figure 3. CPN₁ (a) TEM, (b) HAADF-STEM, and (c–f) EDS images.

Applicability of CPN_x in heterogenous catalysis. To evaluate the activity and stability of the CPN_x materials as lightweight metal-free supports in catalytic reactions at high temperatures, we deposited Cu and Fe nanoparticles on CPN₁. While the typical alloy in CO₂ hydrogenation to methanol is Cu-Zn alloy, the combination of Cu and Fe is much less explored. Then, we studied the catalytic activity of the resulting supported catalyst for CO₂ hydrogenation. We selected CPN₁ as a stable metal-free support on account of its superior resistance to oxidation at high temperatures, good CO₂ adsorption capacity, and small average pore width. A

CuFe/CPN₁ catalyst was synthesized by wet impregnation of CPN₁ with a copper (II) nitrate aqueous solution to obtain a Cu concentration of 7.5 wt%, followed by thermal reduction under a H₂:N₂ (5:95, v/v) atmosphere to afford Cu⁰/CPN₁, and subsequent impregnation of the reduced Cu/CPN₁ with an iron (III) nitrate nonahydrate solution to form 5 wt% of iron content followed by H₂:N₂ (5:95 v/v) reduction treatment. The resulting CuFe/CPN₁ catalyst was washed several times with water and acetone to remove unreacted metal salts. The chemical states of CuFe/CPN₁ were determined via XPS measurements. The presence of a doublet at 933.3 and 952.7 eV in the Cu core-level spectrum shows the formation of CuO, indicating the spontaneous oxidation of Cu nanoparticles upon storage in air (Figure S7a). Another doublet at 936.1 and 955.5 eV, accompanied by satellite peaks at 943.0 and 962.8 eV, is assigned to Cu(OH)₂.³⁹ The Fe 2p electronic configuration is deconvoluted into three doublets, corresponding to FeO and Fe₂O₃ (FeO is associated with the doublet peak at 711.0 and 723.8 eV, Fe₂O₃ with the doublet at 713.4 and 726.3 and its satellite doublet at 717.0 and 728.8 eV) with no evidence for the presence of metallic iron (Figure S7b).⁴⁰ Overall, the XPS C 1s, N 1s, and P 2p spectra of CuFe/CPN₁ show only a few changes after the addition of metal, namely, no amine (–NH–) group is detected in the N 1s spectrum and the peaks are shifted to higher values, probably a reflection of the charge transfer of the CPN₁ to the metal oxide on the sample surface (Figures S7 c–e). The O 1s XPS spectrum verifies the formation of metal oxides and other oxides species mentioned above (Figure S7f). The XRD pattern of CuFe/CPN₁ further confirms the formation of CuFe metallic sites on the CPN₁ support after the reduction treatment (Figure S8). The ICP data reveals a metal loading of 5.98 wt% Cu and 3.02 wt% Fe

on CPN₁. We chose this metal composition to see if the current limitations of Cu/ZnO/Al₂O₃ in terms of low activity and insufficient selectivity can be overcome by a different Cu alloying in a metal-free support. Precedents on the use of Cu-Fe combination for CO₂ hydrogenation to methanol are reported in the literature.^{41,42}

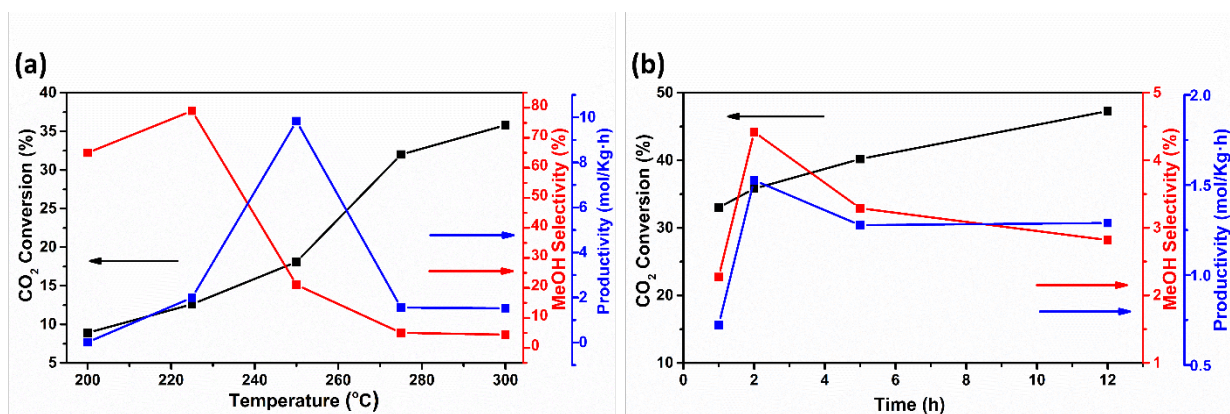


Figure 4. (a) CO₂ conversion, MeOH selectivity and productivity for CO₂ hydrogenation catalyzed by CuFe/CNP₁ for 2 h at different reaction temperatures. (b) Evolution of conversion, selectivity and productivity at a reaction temperature of 300 °C over 12 h. Reaction conditions: 20 bar, 15 mL/min CO₂, 3:1 v:v, H₂:CO₂, 100 mg catalyst.

CuFe/CPN₁ catalyst performance. Considering the presence of Cu and Fe oxide species on the surface revealed by XPS, the catalysts were activated at 300 °C for 1 h under pure hydrogen flow before the reaction to reduce these surface metal-oxides species. The catalysts were then exposed to a flow of 15 mL/min of CO₂ and H₂ (3:1, v:v) at various temperatures in the range 200–300 °C with 20 °C increments. At each temperature the reactor was allowed to equilibrate for 1 h and then the composition of the reaction mixture was analyzed by gas chromatography

in triplicate at 15 min interval. Differences in the three measurements were lesser than 10%. The main reaction products, methanol, ethanol, and methane, were accompanied by lesser amounts of ethane and CO.

The results of the activity test for CuFe/CPN1 regarding CO₂ conversion and methanol selectivity are summarized in Figure 4a. As expected, CO₂ conversion increased with temperature, from 8.9% (at 200 °C) to 35.8% (at 300 °C). In contrast, methanol selectivity exhibited the inverse trend. However, due to the higher CO₂ conversion, the CH₃OH production rate also increased as a function of temperature, from 0.015 to 9.82 mol_{CH₃OH} kg_{cat}⁻¹ h⁻¹ at reaction temperatures of 200 to 300 °C, respectively. At 200 °C, when CO₂ conversion was 9.3%, the major product was methanol (65%), accompanied by a rather notable percentage of ethanol (26%), giving a remarkable combined alcohol selectivity over 90%. The maximum methanol selectivity was achieved at 225 °C (79%) and a CO₂ conversion of 12.6%. However, at 250 °C, the main product was CH₄ (76%), and CH₃OH selectivity decreased to 21%. Further increasing the reaction temperature resulted in lower MeOH selectivity, with methane as the major product. Interestingly, CO selectivity was consistently below 5% in the temperature range under study. Control experiments using CPN₁ in the absence of Cu and Fe revealed no catalytic activity under the same conditions, indicating that Cu and Fe are the active sites.

The catalytic data achieved with CuFe/CPN₁ compare favorably with data report in the literature. Table S4 in the supplementary information provides a summary of reported data relevant to provide a valid assessment of the CuFe/CPN₁ performance. Thus, for instance, for

Cu-Fe alloy supported on Al₂O₃ or Al₂O₃/CeO₂ no methanol formation was observed.^{43,44} Cu/Fe₂O₃ afforded at 230 °C only 6.3% methanol selectivity at a CO₂ conversion of 6.6%.⁴⁵ The data presented in Figure 4 are similar, but still better, than those typically reported for the Cu-Zn alloys. As an example, Cu/ZnO/ZrO₂ exhibits at 240 °C a CO₂ conversion of 17.6% with a 49% methanol selectivity.⁴⁶ It is proposed that the catalytic performance of CuFe/CPN₁ is due to the activity of Cu-Fe alloy with a strong interaction with the CPN₁ support as indicated by XPS binding energy. In addition, H₂ activation is easier, forming metal hydride species spilt over the metal nanoparticle surface. CO₂ adsorption on basic sites will lead to the formation of surface-bound HCOO* species that subsequently will form metal-bound CO· species on the way to CH₃O· intermediates.^{47,48}

Importantly, the CuFe/CPN₁ stability after extended use was confirmed by a catalytic test carried out at 300 °C for 12 h (Figure 4 b). CO₂ conversion increased with time from 33 to 47.3%, and MeOH selectivity remained acceptably stable during the 12 h experiment. HRTEM images of the CuFe/CPN₁ before and after the reaction evidenced no substantial particle size or shape changes, emphasizing the remarkable stability of CuFe/CPN₁ under these harsh conditions (Figure S9).

Conclusions

The preparation of a stable, lightweight metal-free catalyst support that shows unprecedented oxidation resistance under the harsh conditions of the CO₂ hydrogenation to methanol has been reported. To do so, we designed carbon-phosphorus-nitrogen-based precursors with controllable elemental ratio, morphology and structural properties by using

highly ordered supramolecular assemblies of melamine and phosphoric acid as precursors. Detailed structural analysis and CO₂ adsorption measurements reveal a correlation between the elemental composition of the CPNs and their CO₂ adsorption capability, which benefits CO₂ conversion to methanol. The unique surface features of CPNs also ensure the uniform dispersion of both Cu and Fe nanoparticles on CPN₁ and prevent sintering and the oxidation of the Cu active sites during the reaction. The new CuFe/CPN₁ catalyst exhibits a remarkable methanol production yield of 9.82 mol kg_{cat}⁻¹ h⁻¹ at high temperature and pressure (250 °C, 20 bar). Moreover, thanks to the high thermal stability of the CPN₁ substrate and the strong metal–support interactions provided by its particular elemental composition, the supported CuFe/CPN₁ catalyst exhibits good stability throughout a 12 h experiment under harsh conditions.

ASSOCIATED CONTENT

Supporting Information. EA of MPA_x, characterization of CPN_x (XRD, FTIR, EA, XPS, CO₂ full isotherm, N₂ sorption measurements), stability of CPN_x (TGA under air), additional characterization of CPN₁ substrate (³¹P and ¹³C CP MAS NMR), CuFe/CPN₁ catalyst characterization (XPS, XRD, TEM) and comparison of the catalytic activity of CuFe/CPN₁ with related catalysts.

AUTHOR INFORMATION

Corresponding Author

*Prof. Menny Shalom – Department of Chemistry and Ilse Katz Institute for Nanoscale Science and Technology, Ben-Gurion University of the Negev, Beer-Sheva 8410501, Israel.

Email- mennysh@bgu.ac.il

Author Contributions

The manuscript was written through contributions of all authors. All authors have given approval to the final version of the manuscript.

Funding Sources

This project has received funding from the European Research Council (ERC) under the European Union's Horizon 2020 Research and Innovation Programme (grant agreement No. [849068]). The research was partly funded by the following: the Planning & Budgeting Committee/Israel Council for Higher Education (CHE) and Fuel Choice Initiative (Prime Minister Office of Israel), within the framework of "Israel National Research Center for Electrochemical Propulsion" (INREP); the Minerva Center No. 117873; the Israel Science Foundation grant No. 601/21; the Spanish Ministerio de Economía y Competitividad (MAT2016-77608-C3-1-P, MAT2016-75883-C2-2- P); J. A. and H. G. also gratefully acknowledge Financial support from the Spanish Ministry of Economy and Competitiveness (Severo Ochoa SEV2016-0683 and RTI2018-89023-CO2- R1) and by the Generalitat Valenciana (Prometeo 2017-083).

Notes

There are no conflicts to declare.

ACKNOWLEDGMENT

The authors would like to thank Dr. Natalya Froumin and Dr. Keren Keinan-Adamsky for analytical XPS and solid-state NMR, respectively.

REFERENCES

- (1) Bai, S.-T.; De Smet, G.; Liao, Y.; Sun, R.; Zhou, C.; Beller, M.; Maes, B. U. W.; Sels, B. F.

- Homogeneous and Heterogeneous Catalysts for Hydrogenation of CO₂ to Methanol under Mild Conditions. *Chem. Soc. Rev.* **2021**, *50* (7), 4259–4298. <https://doi.org/10.1039/D0CS01331E>.
- (2) Chinese Academy of Sciences. *Thousand-tonne Scale Demonstration of Solar Fuel Synthesis Starts Operation in Lanzhou, China*. https://english.cas.cn/newsroom/research_news/chem/202001/t20200113_229335.shtml (accessed 2022-01-02).
- (3) *The North-C-Methanol project*. <https://northccuhub.eu/north-c-methanol/> (accessed 2022-01-02).
- (4) Ladera, R.; Pérez-Alonso, F. J.; González-Carballo, J. M.; Ojeda, M.; Rojas, S.; Fierro, J. L. G. Catalytic Valorization of CO₂ via Methanol Synthesis with Ga-Promoted Cu–ZnO–ZrO₂ Catalysts. *Appl. Catal. B Environ.* **2013**, *142–143*, 241–248. <https://doi.org/https://doi.org/10.1016/j.apcatb.2013.05.019>.
- (5) Wang, W.-H.; Himeda, Y.; Muckerman, J. T.; Manbeck, G. F.; Fujita, E. CO₂ Hydrogenation to Formate and Methanol as an Alternative to Photo- and Electrochemical CO₂ Reduction. *Chem. Rev.* **2015**, *115* (23), 12936–12973. <https://doi.org/10.1021/acs.chemrev.5b00197>.
- (6) Studt, F.; Sharafutdinov, I.; Abild-Pedersen, F.; Elkjær, C. F.; Hummelshøj, J. S.; Dahl, S.; Chorkendorff, I.; Nørskov, J. K. Discovery of a Ni-Ga Catalyst for Carbon Dioxide

- Reduction to Methanol. *Nat. Chem.* **2014**, *6* (4), 320–324.
<https://doi.org/10.1038/nchem.1873>.
- (7) Kleinman, L.; Bylander, D. M. Efficacious Form for Model Pseudopotentials. *Phys. Rev. Lett.* **1982**, *48* (20), 1425–1428. <https://doi.org/10.1103/PhysRevLett.48.1425>.
- (8) Li, J.; Du, T.; Li, Y.; Jia, H.; Wang, Y.; Song, Y.; Fang, X. Novel Layered Triple Hydroxide Sphere CO₂ Adsorbent Supported Copper Nanocluster Catalyst for Efficient Methanol Synthesis via CO₂ Hydrogenation. *J. Catal.* **2022**, *409*, 24–32.
<https://doi.org/10.1016/j.jcat.2022.03.020>.
- (9) Li, K.; Chen, J. G. CO₂ Hydrogenation to Methanol over ZrO₂-Containing Catalysts: Insights into ZrO₂ Induced Synergy. *ACS Catal.* **2019**, *9* (9), 7840–7861.
<https://doi.org/10.1021/acscatal.9b01943>.
- (10) Bart, J. C. J.; Sneed, R. P. A. Copper-Zinc Oxide-Alumina Methanol Catalysts Revisited. *Catal. Today* **1987**, *2* (1), 1–124. [https://doi.org/https://doi.org/10.1016/0920-5861\(87\)80001-9](https://doi.org/https://doi.org/10.1016/0920-5861(87)80001-9).
- (11) Rungtaweewanit, B.; Baek, J.; Araujo, J. R.; Archanjo, B. S.; Choi, K. M.; Yaghi, O. M.; Somorjai, G. A. Copper Nanocrystals Encapsulated in Zr-Based Metal–Organic Frameworks for Highly Selective CO₂ Hydrogenation to Methanol. *Nano Lett.* **2016**, *16* (12), 7645–7649. <https://doi.org/10.1021/acs.nanolett.6b03637>.
- (12) Witton, T.; Numpilai, T.; Phongamwong, T.; Donphai, W.; Boonyuen, C.; Warakulwit,

- C.; Chareonpanich, M.; Limtrakul, J. Enhanced Activity, Selectivity and Stability of a CuO-ZnO-ZrO₂ Catalyst by Adding Graphene Oxide for CO₂ Hydrogenation to Methanol. *Chem. Eng. J.* **2018**, *334*, 1781–1791. <https://doi.org/https://doi.org/10.1016/j.cej.2017.11.117>.
- (13) Tada, S.; Fujiwara, K.; Yamamura, T.; Nishijima, M.; Uchida, S.; Kikuchi, R. H. Ahouari, A. Soualah, A. Le Valant, L. Pinard, P. Magnoux and Y. Pouilloux, *React. Kinet., Mech. Catal.*, **2013**, *110*, 131–145. *Chem. Eng. J.* **2020**, *381*, 122750. <https://doi.org/https://doi.org/10.1016/j.cej.2019.122750>.
- (14) Ahouari, H.; Soualah, A.; Le Valant, A.; Pinard, L.; Magnoux, P.; Pouilloux, Y. Methanol Synthesis from CO₂ Hydrogenation over Copper Based Catalysts. *React. Kinet. Mech. Catal.* **2013**, *110*(1), 131–145. <https://doi.org/10.1007/s11144-013-0587-9>.
- (15) Liang, B.; Ma, J.; Su, X.; Yang, C.; Duan, H.; Zhou, H.; Deng, S.; Li, L.; Huang, Y. Investigation on Deactivation of Cu/ZnO/Al₂O₃ Catalyst for CO₂ Hydrogenation to Methanol. *Ind. Eng. Chem. Res.* **2019**, *58* (21), 9030–9037. <https://doi.org/10.1021/acs.iecr.9b01546>.
- (16) Karelovic, A.; Ruiz, P. The Role of Copper Particle Size in Low Pressure Methanol Synthesis via CO₂ Hydrogenation over Cu/ZnO Catalysts. *Catal. Sci. Technol.* **2015**, *5* (2), 869–881. <https://doi.org/10.1039/C4CY00848K>.
- (17) Du, S.; Tang, W.; Lu, X.; Wang, S.; Guo, Y.; Gao, P.-X. *J. Power Source* **274** (2015) 619–

628. *Adv. Mater. Interfaces* **2018**, *5* (3), 1700730.
<https://doi.org/https://doi.org/10.1002/admi.201700730>.
- (18) Zhang, Y.; Yao, D.; Xia, B.; Jaroniec, M.; Ran, J.; Qiao, S.-Z. Photocatalytic CO₂ Reduction: Identification and Elimination of False-Positive Results. *ACS Energy Lett.* **2022**, *7*(5), 1611–1617. <https://doi.org/10.1021/acsenergylett.2c00427>.
- (19) Ud Din, I.; Shaharun, M. S.; Subbarao, D.; Naeem, A. Synthesis, Characterization and Activity Pattern of Carbon Nanofibers Based Copper/Zirconia Catalysts for Carbon Dioxide Hydrogenation to Methanol: Influence of Calcination Temperature. *J. Power Sources* **2015**, *274*, 619–628.
<https://doi.org/https://doi.org/10.1016/j.jpowsour.2014.10.087>.
- (20) Fan, Y. J.; Wu, S. F. A Graphene-Supported Copper-Based Catalyst for the Hydrogenation of Carbon Dioxide to Form Methanol. *J. CO₂ Util.* **2016**, *16*, 150–156.
<https://doi.org/https://doi.org/10.1016/j.jcou.2016.07.001>.
- (21) Chen, X.; He, F.; Shen, Y.; Yang, Y.; Mei, H.; Liu, S.; Mori, T.; Zhang, Y. Effect of Carbon Supports on Enhancing Mass Kinetic Current Density of Fe-N/C Electrocatalysts. *Chem. – A Eur. J.* **2017**, *23* (58), 14597–14603.
<https://doi.org/https://doi.org/10.1002/chem.201703020>.
- (22) Azoulay, A.; Barrio, J.; Tzadikov, J.; Volokh, M.; Albero, J.; Gervais, C.; Amo-Ochoa, P.; García, H.; Zamora, F.; Shalom, M. Synthesis of Metal-Free Lightweight Materials with

- Sequence-Encoded Properties. *J. Mater. Chem. A* **2020**, *8* (17), 8752–8760.
<https://doi.org/10.1039/D0TA03162C>.
- (23) Duan, C.; Yuan, D.; Yang, Z.; Li, S.; Tao, L.; Wang, Q.; Wang, T. High Wear-Resistant Performance of Thermosetting Polyimide Reinforced by Graphitic Carbon Nitride (g-C₃N₄) under High Temperature. *Compos. Part A Appl. Sci. Manuf.* **2018**, *113*, 200–208.
<https://doi.org/https://doi.org/10.1016/j.compositesa.2018.07.008>.
- (24) Barrio, J.; Barzilai, S.; Karjule, N.; Amo-Ochoa, P.; Zamora, F.; Shalom, M. Fluorescent Carbon Nitride Macrostructures Derived from Triazine-Based Cocrystals. *Adv. Opt. Mater.* **2021**, *9*(19), 2100683. <https://doi.org/https://doi.org/10.1002/adom.202100683>.
- (25) Barrio, J.; Lin, L.; Amo-Ochoa, P.; Tzadikov, J.; Peng, G.; Sun, J.; Zamora, F.; Wang, X.; Shalom, M. Unprecedented Centimeter-Long Carbon Nitride Needles: Synthesis, Characterization and Applications. *Small* **2018**, *14* (21), 1800633.
<https://doi.org/10.1002/sml.201800633>.
- (26) Stein, P.; Dickson, M. K.; Roundhill, D. M. Raman and Infrared Spectra of Binuclear Platinum(II) and Platinum(III) Octaphosphite Complexes. A Characterization of the Intermetallic Bonding. *J. Am. Chem. Soc.* **1983**, *105* (11), 3489–3494.
<https://doi.org/10.1021/ja00349a020>.
- (27) Mirzayi, M.; Hekmatshoar, M. H. Optical and IR Study of Li₂O–CuO–P₂O₅ Glasses. *Ionics (Kiel)*. **2009**, *15*(1), 121–127. <https://doi.org/10.1007/s11581-008-0247-7>.

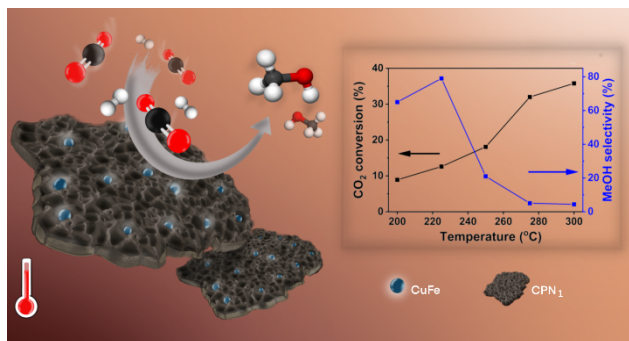
- (28) Gibot, P.; Schnell, F.; Spitzer, D. Enhancement of the Graphitic Carbon Nitride Surface Properties from Calcium Salts as Templates. *Microporous Mesoporous Mater.* **2016**, *219*, 42–47. <https://doi.org/https://doi.org/10.1016/j.micromeso.2015.07.026>.
- (29) Liu, Y.; Gao, P.; Zhang, T.; Zhu, X.; Zhang, M.; Chen, M.; Du, P.; Wang, G.-W.; Ji, H.; Yang, J.; Yang, S. Azide Passivation of Black Phosphorus Nanosheets: Covalent Functionalization Affords Ambient Stability Enhancement. *Angew. Chemie Int. Ed.* **2019**, *58* (5), 1479–1483. <https://doi.org/https://doi.org/10.1002/anie.201813218>.
- (30) Li, Y.; Zhang, H.; Jiang, Y.; Shi, M.; Bawa, M.; Wang, X.; Zhu, S. Assembly of Metallophthalocyanine-Polyoxometalate Hybrid for Highly Efficient Desulfurization of Organic and Inorganic Sulfur under Aerobic Conditions. *Fuel* **2019**, *241*, 861–869. <https://doi.org/https://doi.org/10.1016/j.fuel.2018.12.091>.
- (31) Ge, L.; Han, C.; Xiao, X.; Guo, L.; Li, Y. Enhanced Visible Light Photocatalytic Hydrogen Evolution of Sulfur-Doped Polymeric g-C₃N₄ Photocatalysts. *Mater. Res. Bull.* **2013**, *48* (10), 3919–3925. <https://doi.org/https://doi.org/10.1016/j.materresbull.2013.06.002>.
- (32) Ge, H.; Qi, G.; Kang, E.-T.; Neoh, K. G. Study of Overoxidized Polypyrrole Using X-Ray Photoelectron Spectroscopy. *Polymer (Guildf)*. **1994**, *35* (3), 504–508. [https://doi.org/https://doi.org/10.1016/0032-3861\(94\)90503-7](https://doi.org/https://doi.org/10.1016/0032-3861(94)90503-7).
- (33) Desimoni, E.; Casella, G. I.; Morone, A.; Salvi, A. M. XPS Determination of Oxygen-Containing Functional Groups on Carbon-Fibre Surfaces and the Cleaning of These

- Surfaces. *Surf. Interface Anal.* **1990**, *15* (10), 627–634.
<https://doi.org/https://doi.org/10.1002/sia.740151011>.
- (34) Wilke, A.; Yuan, J.; Antonietti, M.; Weber, J. Enhanced Carbon Dioxide Adsorption by a Mesoporous Poly(Ionic Liquid). *ACS Macro Lett.* **2012**, *1* (8), 1028–1031.
<https://doi.org/10.1021/mz3003352>.
- (35) Xia, Y.; Tian, Z.; Heil, T.; Meng, A.; Cheng, B.; Cao, S.; Yu, J.; Antonietti, M. Highly Selective CO₂ Capture and Its Direct Photochemical Conversion on Ordered 2D/1D Heterojunctions. *Joule* **2019**, *3* (11), 2792–2805.
<https://doi.org/https://doi.org/10.1016/j.joule.2019.08.011>.
- (36) Zeleňák, V.; Badaničová, M.; Halamová, D.; Čejka, J.; Zukal, A.; Murafa, N.; Goerigk, G. Amine-Modified Ordered Mesoporous Silica: Effect of Pore Size on Carbon Dioxide Capture. *Chem. Eng. J.* **2008**, *144*(2), 336–342. <https://doi.org/10.1016/j.cej.2008.07.025>.
- (37) Velencoso, M. M.; Battig, A.; Markwart, J. C.; Schartel, B.; Wurm, F. R. Molecular Firefighting—How Modern Phosphorus Chemistry Can Help Solve the Challenge of Flame Retardancy. *Angew. Chemie - Int. Ed.* **2018**, *57* (33), 10450–10467.
<https://doi.org/10.1002/anie.201711735>.
- (38) Sannigrahi, P.; Ingall, E. Polyphosphates as a Source of Enhanced P Fluxes in Marine Sediments Overlain by Anoxic Waters: Evidence from ³¹P NMR. *Geochem. Trans.* **2005**, *6*(3), 52. <https://doi.org/10.1186/1467-4866-6-52>.

- (39) Chao, S.-J.; Tsai, M.-H.; Yu, R.-P.; Hua, L.-C.; Hu, C.-C.; Huang, C. Dezincification of Brass Water Meters in a Long-Term Study: Effects of Anions, Alkalinity, and Residual Chlorine. *Environ. Sci. Water Res. Technol.* **2021**, *7* (9), 1666–1676. <https://doi.org/10.1039/D1EW00351H>.
- (40) Zhang, R.; Li, Y.; Zhen, T. Ammonia Selective Catalytic Reduction of NO over Fe/Cu-SSZ-13. *RSC Adv.* **2014**, *4* (94), 52130–52139. <https://doi.org/10.1039/C4RA09290B>.
- (41) Kiatphuengporn, S.; Chareonpanich, M.; Limtrakul, J. Effect of Unimodal and Bimodal MCM-41 Mesoporous Silica Supports on Activity of Fe–Cu Catalysts for CO₂ Hydrogenation. *Chem. Eng. J.* **2014**, *240*, 527–533. <https://doi.org/https://doi.org/10.1016/j.cej.2013.10.090>.
- (42) Tursunov, O.; Kustov, L.; Kustov, A. A Brief Review of Carbon Dioxide Hydrogenation to Methanol Over Copper and Iron Based Catalysts. *Oil Gas Sci. Technol. – Rev. d'IFP Energies Nouv.* **2017**, *72* (5), 30. <https://doi.org/10.2516/ogst/2017027>.
- (43) Pastor-Pérez, L.; Baibars, F.; Le Sache, E.; Arellano-García, H.; Gu, S.; Reina, T. R. CO₂ Valorisation via Reverse Water-Gas Shift Reaction Using Advanced Cs Doped Fe-Cu/Al₂O₃ Catalysts. *J. CO₂ Util.* **2017**, *21*, 423–428. <https://doi.org/10.1016/j.jcou.2017.08.009>.
- (44) Yang, L.; Pastor-Pérez, L.; Villora-Pico, J. J.; Gu, S.; Sepúlveda-Escribano, A.; Reina, T. R. CO₂ Valorisation via Reverse Water-Gas Shift Reaction Using Promoted Fe/CeO₂-

- Al₂O₃ Catalysts: Showcasing the Potential of Advanced Catalysts to Explore New Processes Design. *Appl. Catal. A Gen.* **2020**, *593*, 117442. <https://doi.org/https://doi.org/10.1016/j.apcata.2020.117442>.
- (45) Lee, K. H.; Lee, J. S. Effects of Catalyst Composition on Methanol Synthesis from CO₂/H₂. *Korean J. Chem. Eng.* **1995**, *12* (4), 460–465. <https://doi.org/10.1007/BF02705811>.
- (46) Arena, F.; Barbera, K.; Italiano, G.; Bonura, G.; Spadaro, L.; Frusteri, F. Synthesis, Characterization and Activity Pattern of Cu–ZnO/ZrO₂ Catalysts in the Hydrogenation of Carbon Dioxide to Methanol. *J. Catal.* **2007**, *249* (2), 185–194. <https://doi.org/https://doi.org/10.1016/j.jcat.2007.04.003>.
- (47) Grabow, L. C.; Mavrikakis, M. Mechanism of Methanol Synthesis on Cu through CO₂ and CO Hydrogenation. *ACS Catal.* **2011**, *1* (4), 365–384. <https://doi.org/10.1021/cs200055d>.
- (48) Frei, M. S.; Capdevila-Cortada, M.; García-Muelas, R.; Mondelli, C.; López, N.; Stewart, J. A.; Curulla Ferré, D.; Pérez-Ramírez, J. Mechanism and Microkinetics of Methanol Synthesis via CO₂ Hydrogenation on Indium Oxide. *J. Catal.* **2018**, *361*, 313–321. <https://doi.org/https://doi.org/10.1016/j.jcat.2018.03.014>.

TOC



Supporting Information

Carbon-phosphorus-nitrogen materials as highly thermally stable catalyst supports for CO₂ hydrogenation to methanol

*Adi Azoulay^a, Alberto Garcia Baldovi^b, Josep Albero^b, Noa Azaria^c, Jonathan Tzadikov^a, Ayelet Tashakory^a, Neeta Karjule^a, Shmuel Hayun^c, Hermenegildo García^b, and Menny Shalom^{*a}*

^aDepartment of Chemistry and Ilse Katz Institute for Nanoscale Science and Technology, Ben-Gurion University of the Negev, Beer-Sheva 8410501, Israel.

^bInstituto Universitario Mixto de Tecnología Química (UPV-CSIC), Universitat Politècnica de València, Avda. de los Narajos s/n, 46022, Valencia, Spain.

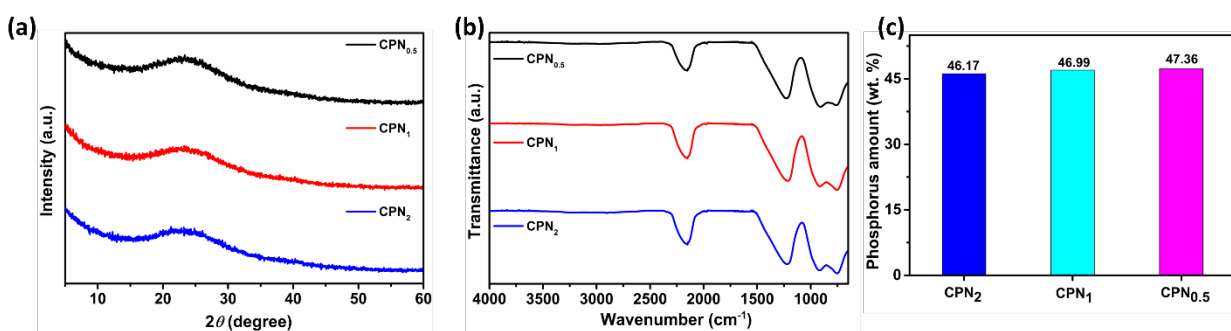
^cDepartment of Materials Engineering, Ben-Gurion University of the Negev, Beer-Sheva, Israel.

*Prof. Menny Shalom – Department of Chemistry and Ilse Katz Institute for Nanoscale Science and Technology, Ben-Gurion University of the Negev, Beer-Sheva 8410501, Israel.

Email- mennysh@bgu.ac.il

Table 1. Elemental analysis data wt% of MPA_x supramolecular precursors.

Element	P	N	C	H	O
MPA ₂	7.83	43.47	18.90	4.83	24.97
MPA ₁	10.82	40.72	17.76	4.46	26.24
MPA _{0.5}	13.49	36.98	16.17	4.12	29.24

**Figure S1.** CPN_x 800 (a) XRD patterns, (b) FTIR spectra, and (c) phosphorous contents(wt %) as determined by ICP-OES.**Table S2.** Elemental analysis data in wt% of CPN_x 800.

Element	P	N	C	H	O
CPN ₂	46.17	39.99	4.67	0.27	8.90
CPN ₁	46.99	39.42	4.41	0.28	8.90
CPN _{0.5}	47.36	37.56	3.85	0.37	10.86

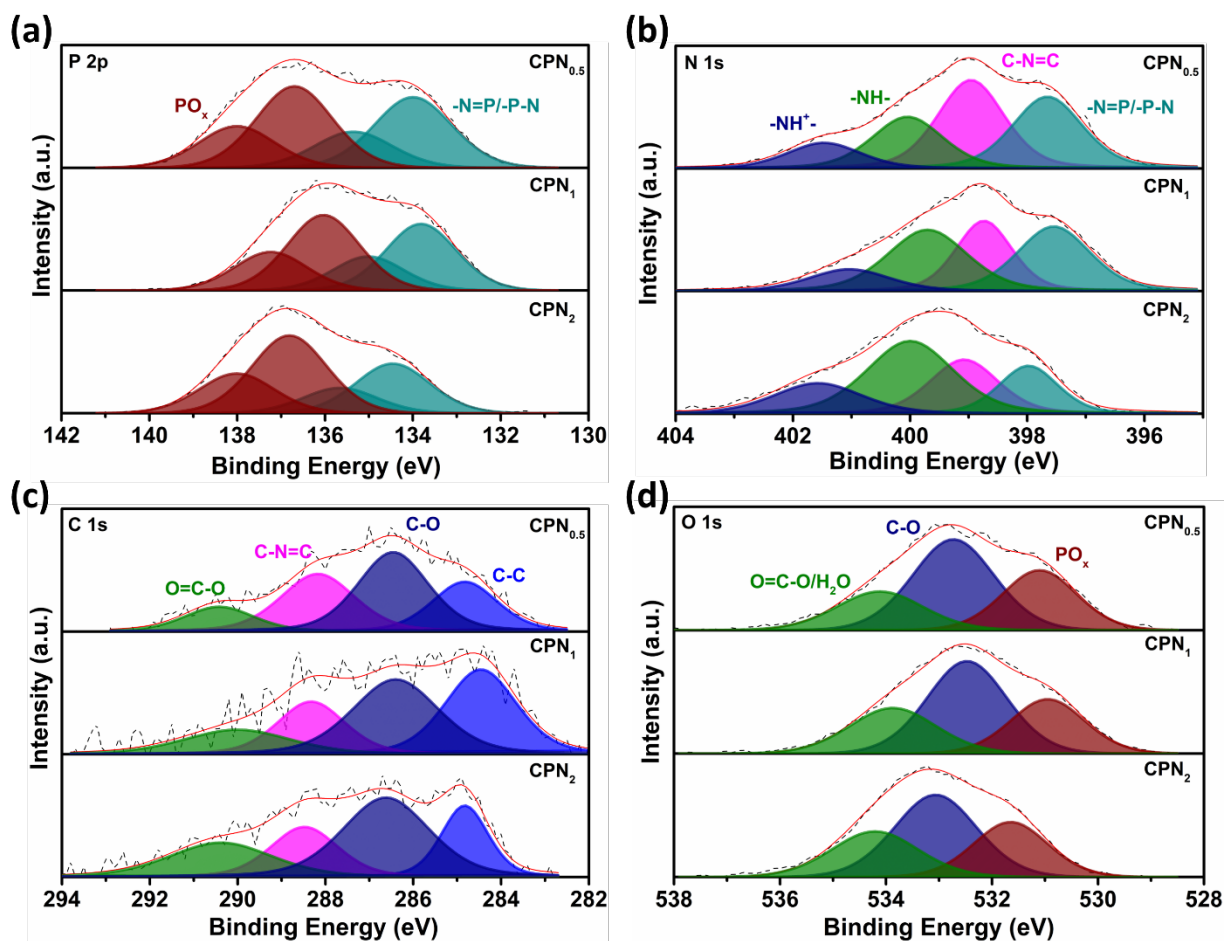


Figure S2. High-resolution XPS spectra of CPN_x 800 materials for (a) P 2p, (b) N 1s, (c) C 1s, and (d) O 1s.

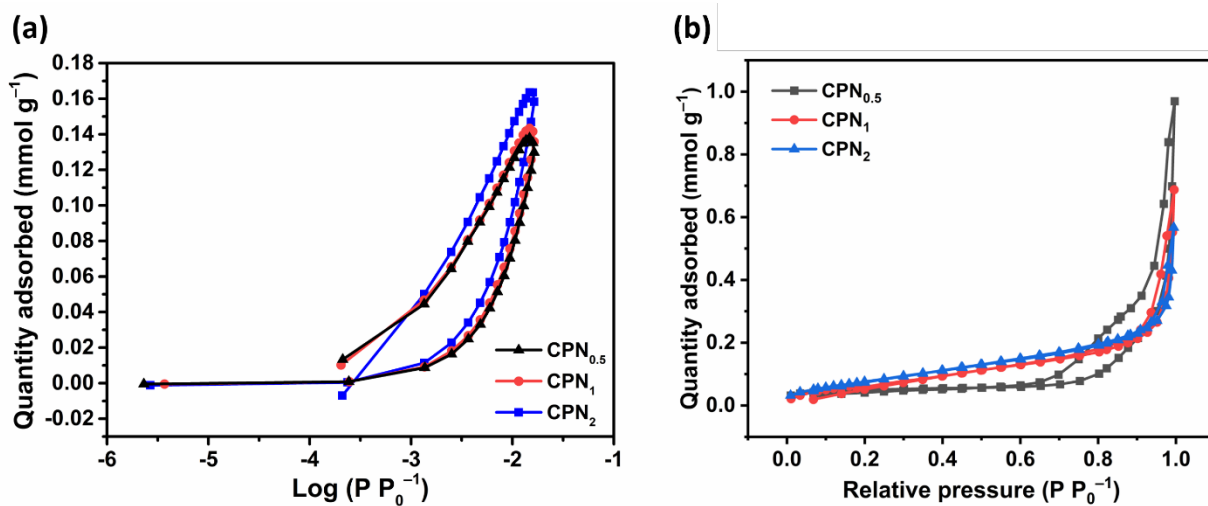


Figure S3. (a) CO₂ adsorption isotherms and (b) N₂ adsorption–desorption isotherms (77 K) of CPN_x materials.

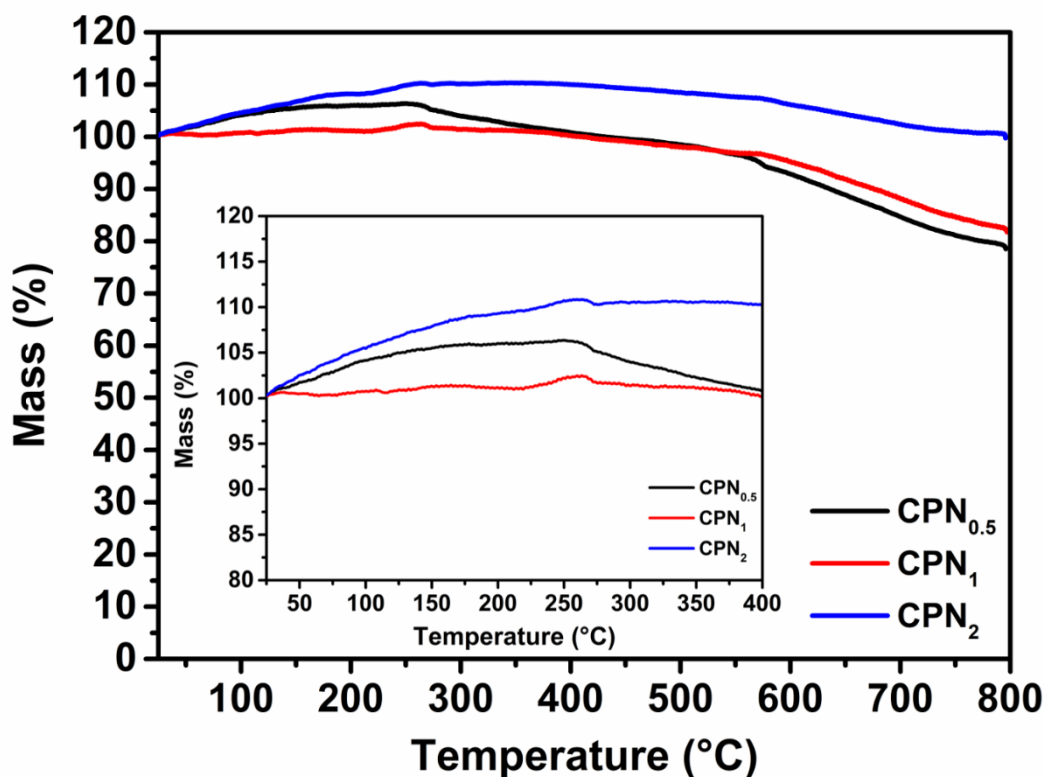


Figure S4. TGA curves under air of CPN_x (inset: magnified view up to 400 °C).

Table S3. BET surface area and average pore width of CPN_x materials.

Material	BET surface area (m ² g ⁻¹)	BJH adsorption average pore width (nm)
CPN ₂	6.84 ± 0.06	10.59
CPN ₁	5.64 ± 0.20	14.09
CPN _{0.5}	3.77 ± 0.08	39.79

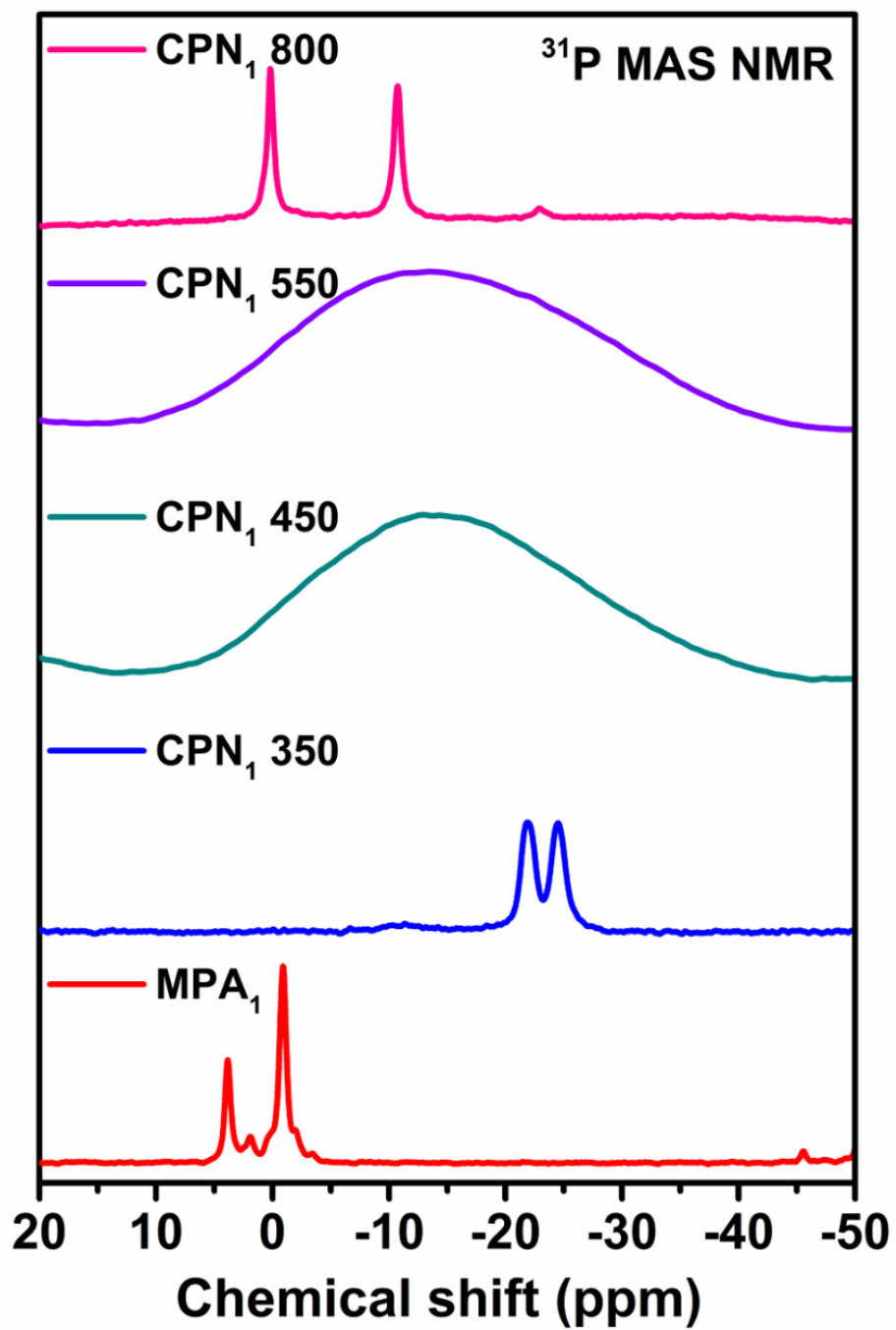


Figure S5. ^{31}P CP MAS NMR spectra of the MPA_1 co-crystal and the products of its calcination at different temperatures.

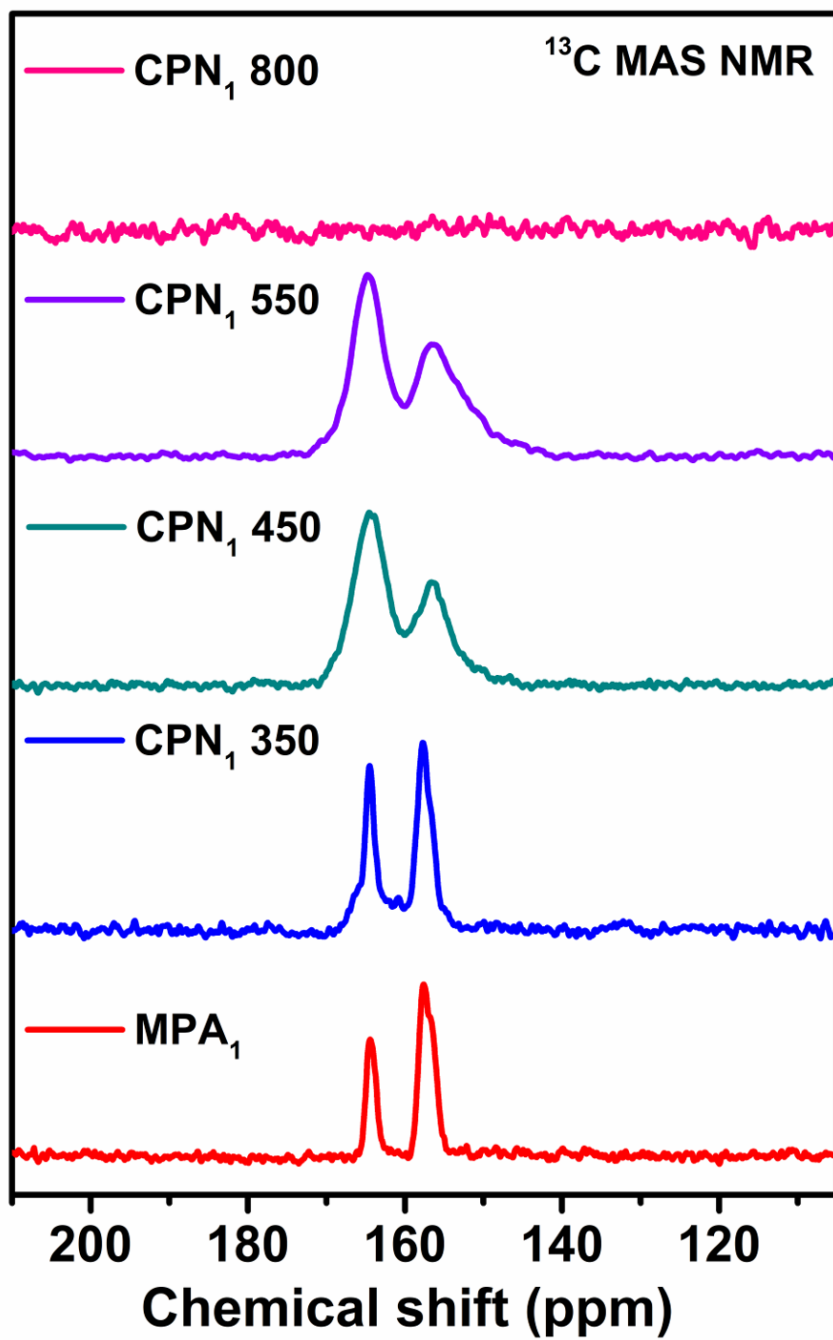


Figure S6. ¹³C CP MAS NMR spectra of the MPA₁ co-crystal and the products of its calcination at different temperatures.

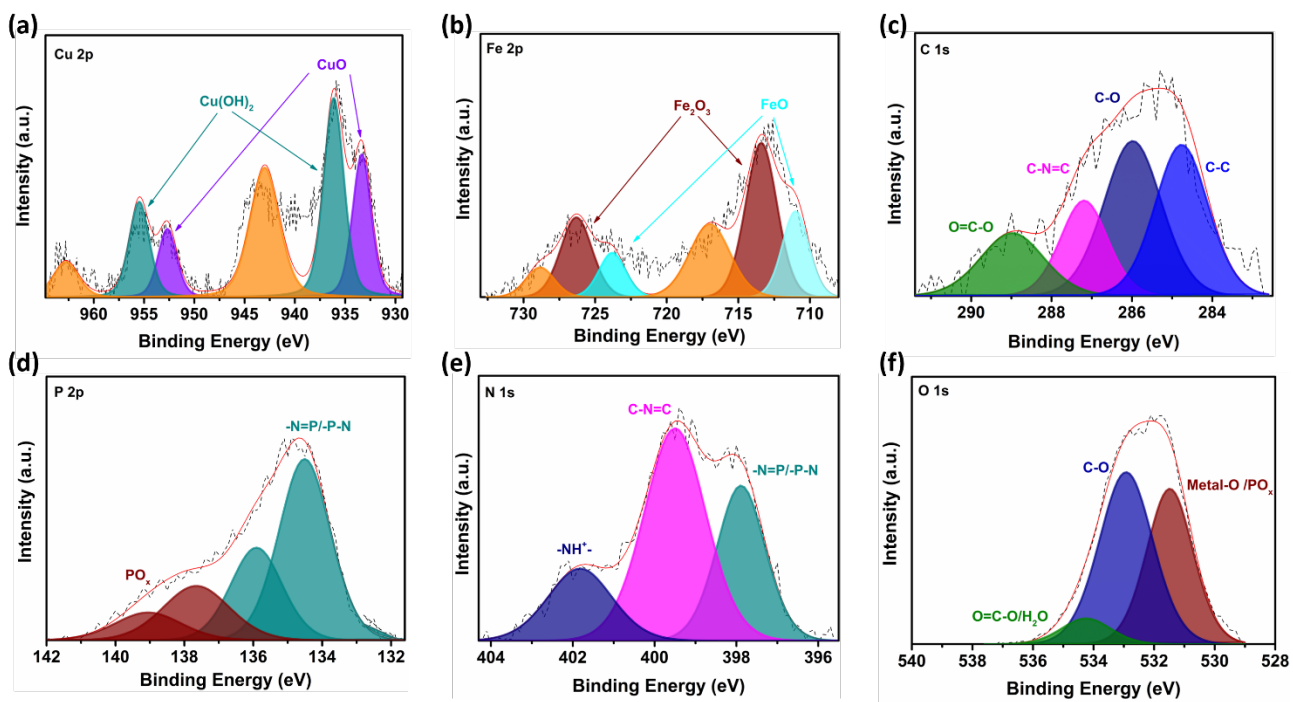


Figure S7. High-resolution XPS spectra of CuFe/CPN₁ for (a) Cu 2p, (b) Fe 2p, (c) C 1s, and (d) P 2p, (e) N 1s and (f) O 1s.

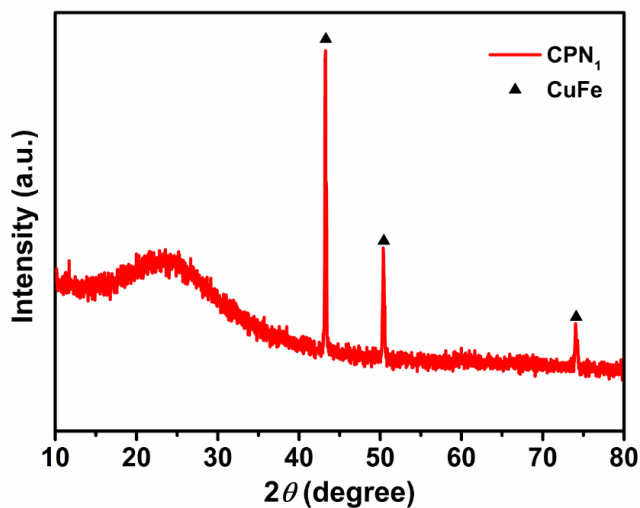


Figure S8. XRD pattern of CuFe/CPN₁. Black triangles: cubic CuFe, PDF 92–152–4702 (ICDD card, 2002 database).

Table S4. Comparison of the catalytic activity of CuFe/CPN₁ with those or related catalysts reported in the literature under analogous conditions.

Catalyst	Reaction T ^a (°C)	P(atm)	H ₂ :CO ₂ ratio	Conv. (%)	MeOH select. (%)	CO selec.(%)	Ref.
Fe-Cu/Al ₂ O ₃	500	1	4	55	-	100	1
Cu-Fe/CeO ₂ -Al ₂ O ₃	500	1	4	45	-	100	2
Cu/MgO-TiO ₂	230	30	3	0.6	30	70	3
Cu/Fe ₂ O ₃	230	30	3	6.3	6.6	25.4	4
Cu-Zn-Ga	240	45	2.8	27	50	-	5
Cu/ZnO/ZrO ₂	240	30	3	17.6	49	-	6
Cu-Zn-Al-Zr	250	50	3	25	48	-	7
CuFe/CPN ₁	225	20	3	12.6	79	< 5	This work

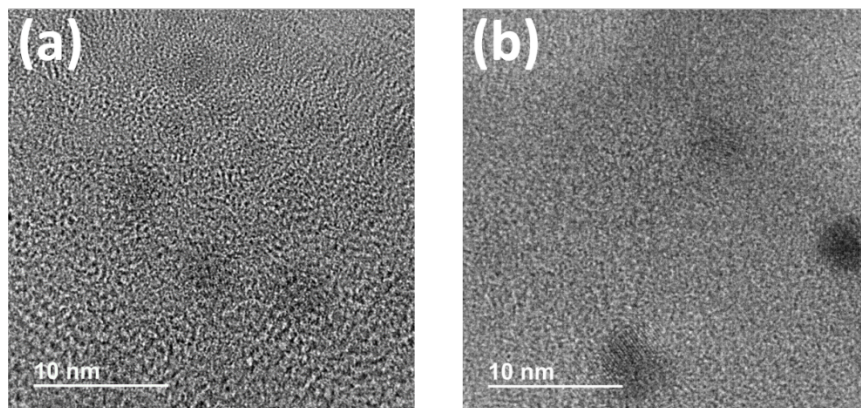


Figure S9. CuFe/CPN₁ TEM images (a) before and (b) after 12 h reaction.

Supporting Information References

- (1) Pastor-Pérez, L.; Baibars, F.; Le Sache, E.; Arellano-García, H.; Gu, S.; Reina, T. R. CO₂ Valorisation via Reverse Water-Gas Shift Reaction Using Advanced Cs Doped Fe-Cu/Al₂O₃ Catalysts. *J. CO₂ Util.* **2017**, *21*, 423–428. <https://doi.org/10.1016/j.jcou.2017.08.009>.
- (2) Yang, L.; Pastor-Pérez, L.; Villora-Pico, J. J.; Gu, S.; Sepúlveda-Escribano, A.; Reina, T. R. CO₂ Valorisation via Reverse Water-Gas Shift Reaction Using Promoted Fe/CeO₂-Al₂O₃ Catalysts: Showcasing the Potential of Advanced Catalysts to Explore New Processes Design. *Appl. Catal. A Gen.* **2020**, *593*, 117442. <https://doi.org/https://doi.org/10.1016/j.apcata.2020.117442>.

- (3) Liu, C.; Guo, X.; Guo, Q.; Mao, D.; Yu, J.; Lu, G. Methanol Synthesis from CO₂ Hydrogenation over Copper Catalysts Supported on MgO-Modified TiO₂. *J. Mol. Catal. A Chem.* **2016**, *425*, 86–93. <https://doi.org/https://doi.org/10.1016/j.molcata.2016.09.032>.
- (4) Lee, K. H.; Lee, J. S. Effects of Catalyst Composition on Methanol Synthesis from CO₂/H₂. *Korean J. Chem. Eng.* **1995**, *12* (4), 460–465. <https://doi.org/10.1007/BF02705811>.
- (5) Li, M. M.-J.; Zeng, Z.; Liao, F.; Hong, X.; Tsang, S. C. E. Enhanced CO₂ Hydrogenation to Methanol over CuZn Nanoalloy in Ga Modified Cu/ZnO Catalysts. *J. Catal.* **2016**, *343*, 157–167. <https://doi.org/https://doi.org/10.1016/j.jcat.2016.03.020>.
- (6) Arena, F.; Barbera, K.; Italiano, G.; Bonura, G.; Spadaro, L.; Frusteri, F. Synthesis, Characterization and Activity Pattern of Cu–ZnO/ZrO₂ Catalysts in the Hydrogenation of Carbon Dioxide to Methanol. *J. Catal.* **2007**, *249* (2), 185–194. <https://doi.org/https://doi.org/10.1016/j.jcat.2007.04.003>.
- (7) Gao, P.; Li, F.; Zhao, N.; Xiao, F.; Wei, W.; Zhong, L.; Sun, Y. Influence of Modifier (Mn, La, Ce, Zr and Y) on the Performance of Cu/Zn/Al Catalysts via Hydrotalcite-like Precursors for CO₂ Hydrogenation to Methanol. *Appl. Catal. A Gen.* **2013**, *468*, 442–452. <https://doi.org/https://doi.org/10.1016/j.apcata.2013.09.026>.